Supporting information for: "Strong gate-tunability of flat bands in bilayer graphene due to moiré encapsulation between hBN monolayers"

Robin Smeyers, Milorad V. Milošević, Lucian Covaci

E-mail: robin.smeyers@uantwerpen.be, milorad.milosevic@uantwerpen.be, lucian.covaci@uantwerpen.be

Department of Physics and NANOlab Center of Excellence, University of Antwerp, Groenenborgerlaan 171, 2020 Antwerp, Belgium

1. Analysis of moiré terms

In this section we provide a numerical analysis of the different terms present in the effective moiré potential. The moiré potential that emerges from placing a single hBN layer onto a single graphene layer is given in general by [1]:

$$U_{eff}(\mathbf{r}) = vG(u_0 f_1 + \tilde{u}_0 f_2)\sigma_0 + \zeta vG(u_3 f_1 + \tilde{u}_3 f_2)\sigma_3$$
$$+ \zeta v\left[\hat{\mathbf{z}} \times \nabla(u_1 f_2 + \tilde{u}_1 f_1) + \nabla(u_2 f_2 + \tilde{u}_2 f_1)\right] \cdot \sigma.$$

$$(1)$$

where

$$(f_1(\mathbf{r}), f_2(\mathbf{r})) = \sum_m \left(1, i(-1)^{m-1}\right) \exp\left(i\mathbf{G}_m \cdot \mathbf{r}\right) \tag{2}$$

are the even and odd periodic functions in which the potential can be decomposed and ζ is the valley index. The first term is the scalar potential, the second term describes the mass term indicating the potential difference between the A and B sublattice, and the third term represents the pseudo-vector potential due to the local modification of the interlayer hopping values. u_i and $\tilde{u}_i$ are the even and odd part of the corresponding Pauli decomposition in matrices σ_i and where $\sigma = [\zeta\sigma_1, \sigma_2]$.

Since we are mainly interested in the electronic properties at low energy we can now switch to the 2-component model for AB-stacked BLG and ABC-stacked TLG in the basis of its corresponding low-energy sites. The low-energy sites are in both cases located on top and bottom layer. The transformation to the low energy model is almost identical for both systems so that here we will only derive the low-energy model for BLG [2] and the one for TLG can be derived in an analogous way as described in Ref. [3]. We can split up the original Hamiltonian for BLG into components $\theta = (\psi_{A1}, \psi_{B2})$ and $\chi = (\psi_{A2}, \psi_{B1})$ for the low- and high-energy sites of the system:

$$\left(\begin{bmatrix} h_\theta & D^\dagger \\ D & h_\chi \end{bmatrix} + U_{t+b}\right) \begin{bmatrix} \theta \\ \chi \end{bmatrix} = E \begin{bmatrix} \theta \\ \chi \end{bmatrix}, \tag{3}$$

where U_{t+b} is a 4×4 matrix representing the applied moiré potential on top and bottom layer in the same basis (A1, B2, A2, B1):

$$U_{t+b} = \begin{bmatrix} V_b(\mathbf{r}) + M_b(\mathbf{r}) & 0 & 0 & A_{1,2}(\mathbf{r}) \\ 0 & V_t(\mathbf{r}) - M_t(\mathbf{r}) & A_{4,3}(\mathbf{r}) & 0 \\ 0 & A_{3,4}(\mathbf{r}) & V_t(\mathbf{r}) + M_t(\mathbf{r}) & 0 \\ A_{2,1}(\mathbf{r}) & 0 & 0 & V_b(\mathbf{r}) - M_b(\mathbf{r}) \end{bmatrix} = \begin{bmatrix} V_{1,1} & V_{2,1}^\dagger \\ V_{2,1} & V_{2,2} \end{bmatrix} \tag{4}$$

Here $V_i(\mathbf{r})$, $M_i(\mathbf{r})$ and $A_{k,l}(\mathbf{r})$ are the scalar, mass and vector potentials from equation 1. The moiré potential splits up into a block-form where the scalar and mass terms appear together on the diagonal and the vector potential terms appear on the off-diagonal blocks. We can further reduce equation 3 to an equation in the low-energy eigenstates θ and by expanding until first order around low E:

$$\left(h_\theta + V_{1,1} - (D + V_{2,1})^\dagger (h_\chi + V_{2,2})^{-1} (D + V_{2,1})\right)\theta = E\tilde{Q}\theta \tag{5}$$

$$\left(\tilde{h}_\theta - \tilde{D}^\dagger \tilde{h}_\chi^{-1}\tilde{D}\right)\theta = E\tilde{Q}\theta \tag{6}$$

Where:

$$\tilde{Q} = 1 + \tilde{D}^\dagger \tilde{h}_\chi^{-2}\tilde{D} \tag{7}$$
$$\tilde{h}_\theta = h_\theta + V_{1,1} \tag{8}$$
$$\tilde{h}_\chi = h_\chi + V_{2,2} \tag{9}$$
$$\tilde{D} = D + A_{2,1} \tag{10}$$

From equation (6) we can identify that $V_{1,1}$, containing the added on-site potential on the low-energy sites is the main contribution in the moiré potential and that the vector potentials and on-site potentials on the high-energy sites are a higher order correction. In light of this we further discuss the effects of the $V_{1,1}$-term which can now again be decomposed into a scalar and a mass term, with the latter being the potential difference between the low-energy sites. We get in the most general form:

$$\tilde{V}(\mathbf{r}) = V_0 + S_V(\mathbf{r}), \tag{11}$$
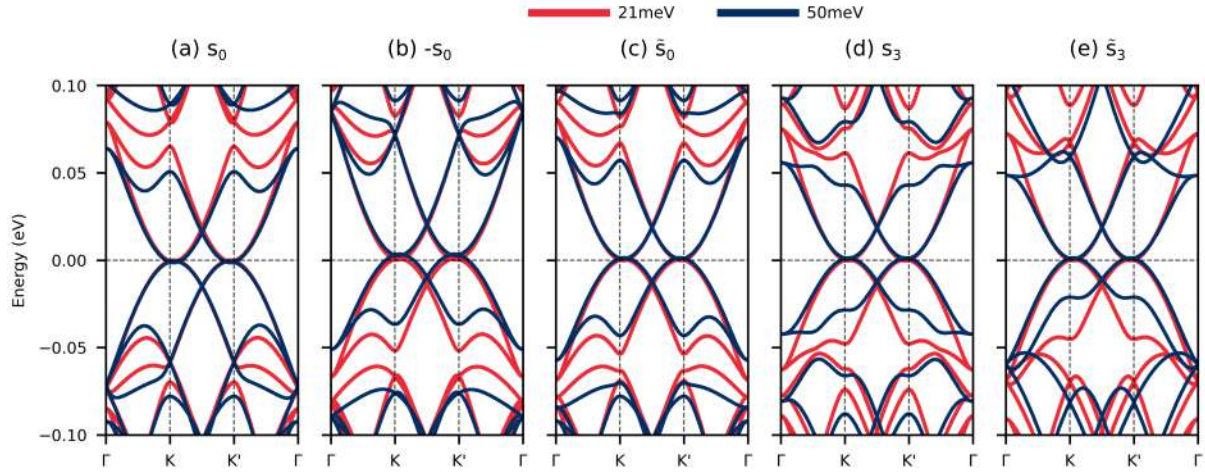$$\tilde{M}(\mathbf{r}) = M_0 + S_M(\mathbf{r}), \tag{12}$$

Figure 1. Band structure of an AB BLG supercell upon which a periodic potential has been applied that corresponds to the different moiré perturbation terms of the 2-component model. The potential is only applied on the low-energy sites with an amplitude of 21 meV (red) and 50 meV (blue). (a) The applied potential is strictly even and of the form $\sum_i V_0 \cos(\mathbf{G}_i.\mathbf{r})$ and identical on both layers. (b) The same as (a) but with a negative sign. (c) The applied potential is of the form $\sum_i V_0 \sin(\mathbf{G}_i.\mathbf{r})$ and with the same sign between both layers. (d) Potential is of the form $\sum_i V_0 \cos(\mathbf{G}_i.\mathbf{r})$ that is opposite on both layers. (e) The potential is of the form $\sum_i V_0 \sin(\mathbf{G}_i.\mathbf{r})$ and with opposite sign between both layers.

where V_0 and M_0 are a constant for the scalar and mass term and $S_V(\mathbf{r})$ and $S_M(\mathbf{r})$ are the spatially varying parts with period of the original moiré potential as no twist is applied between the layers. V_0 will cause a general shift of the spectrum, while M_0 will generate a bandgap at the primary Dirac point (PDP) due to breaking of sublattice symmetry. The spatially varying parts of the 2-component model can be split up into even and odd components just like in equation (1):

$$S_V(\mathbf{r}) = v_{mult} G(s_0 f_1 + \tilde{s}_0 f_2)\sigma_0, \tag{13}$$

$$S_M(\mathbf{r}) = v_{mult} G(s_3 f_1 + \tilde{s}_3 f_2)\sigma_3. \tag{14}$$

Here we provide a numerical analysis of the different components in equation (14) and (13) by applying the appropriate spatially varying potential onto a pristine BLG in the moiré unit cell. Our main point of interest is the behaviour of the gap at the secondary Dirac point (SDP) and how it is modified. It is important to note that for aligned monolayer graphene on hBN an analytical expression for the gap at the SPD has previously been derived [4].

In figure 1 the bandstructure of AB-stacked BLG in the moiré unit cell of unrotated graphene/hBN is given upon which a periodic potential is applied that corresponds with the different contributions in (13) and (14). The s_0 term is the even part of the scalar potential and shows a gap only on the electron side or the hole side depending on the sign of the potential, suggesting that most electron-hole asymmetry comes from this term. The $\tilde{s}_0$ is the odd part of the scalar potential and shows the formation of a gap
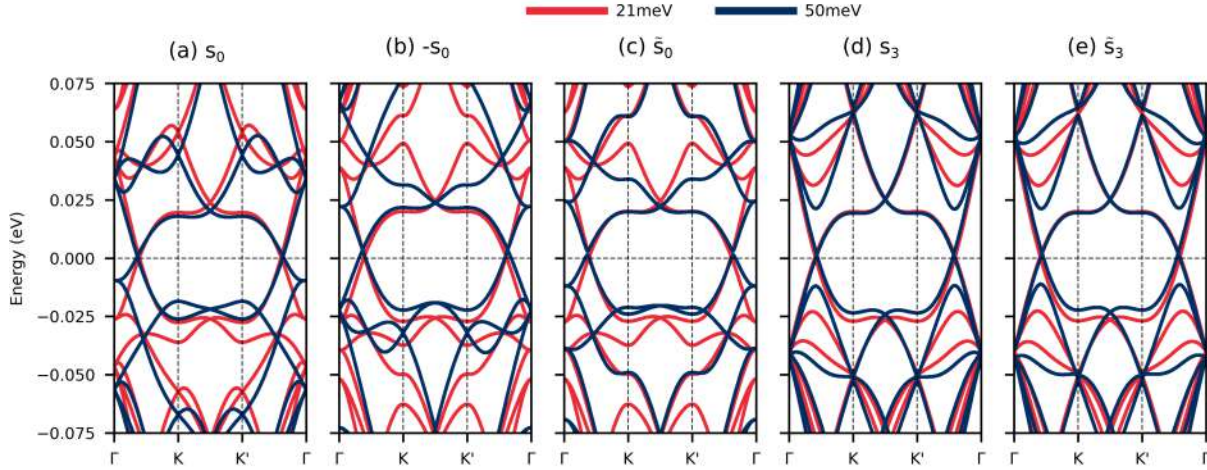
Figure 2. Band structure of an ABC TLG supercell upon which a periodic potential has been applied that corresponds to the different moiré perturbation terms of the 2-component model. The potential is only applied on the low-energy sites with an amplitude of 21 meV (red) and 50 meV (blue). (a) The applied potential is strictly even and of the form $\sum_i V_0 \cos(\mathbf{G}_i.\mathbf{r})$ and identical on both layers. (b) The same as (a) but with a negative sign. (c) The applied potential is of the form $\sum_i V_0 \sin(\mathbf{G}_i.\mathbf{r})$ and with opposite sign between both layers. (d) Potential of the form $\sum_i V_0 \cos(\mathbf{G}_i.\mathbf{r})$ that is identical on both layers. (e) The potential is of the form $\sum_i V_0 \sin(\mathbf{G}_i.\mathbf{r})$ and with opposite sign between both layers.

at the SDP that is equal in magnitude for hole and electron side. The even part of the mass term is given by s_3 and again shows the formation of a gap at the SDP that is largely preserving the electron-hole symmetry and inducing flatter band edges. Lastly we have $\tilde{s}_3$ which is the odd part of the mass term and shows no induced gap at the SDP. The mass term in general appears to induce some strong modification of the bands near the K-point in the first valence band for $\tilde{s}_3$ and in both valence and conduction band for s_3. The only term that is sign-dependent is s_0, which is easy to understand since the odd functions are by definition equal in magnitude and shape for positive and negative regions and the mass term is also only dependent on the absolute difference in potentials which a switch of sign will not change.

The same procedure is applied to an ABC-stacked TLG in the moiré unit cell for which the band structures are shown in figure 2. None of the contributions seems to open up a gap at the PDP or SDP, only a constant average mass term can open a gap at the PDP or perhaps the introduction of a intra- or interlayer pseudo-vector potential, which we do not consider here.

In what follows, the terms in equation (13) and (14) are determined by setting up a continuum model for the graphene/hBN potential for each layer (see ref. [5] for details) and applying the above procedure for the hBN encapsulated systems in the main text. A cut along the y-axis of the 2D moiré potentials are shown in figure 3 for the BLG systems and figure 4 for the TLG systems. The AB1 BLG system, being the focus of the main text, shows a strong s_3 component, inducing a gap in the hole

side and reducing the Fermi velocity near the SDP as is apparent from figure 1 and readily observed in the fully atomistic result of the main text. The potentials for AB1 as described by equations (13) and (14) and figure 3 are added to a BLG in a moiré unit cell for which we calculate the band structure and find a good agreement with the fully atomistic result. The BLG/hBN system also shows a large s_3 contribution which is observed when the band structure is calculated with the simplified model. unlike AB1 however, BLG/hBN shows no such feature in the atomistic result from the main text. Although a reasonable qualitative agreement is reached, some important features such as gaps at the SDP are not always consistently obtained when comparing the 2 methods. We conclude that the additional terms in equation (6) should be included in order to obtain an accurate analytical result. This model does however show the degree of tunability of the moiré pattern onto a multilayer graphene, simply by considering the precise positioning of aligned hBN layers.
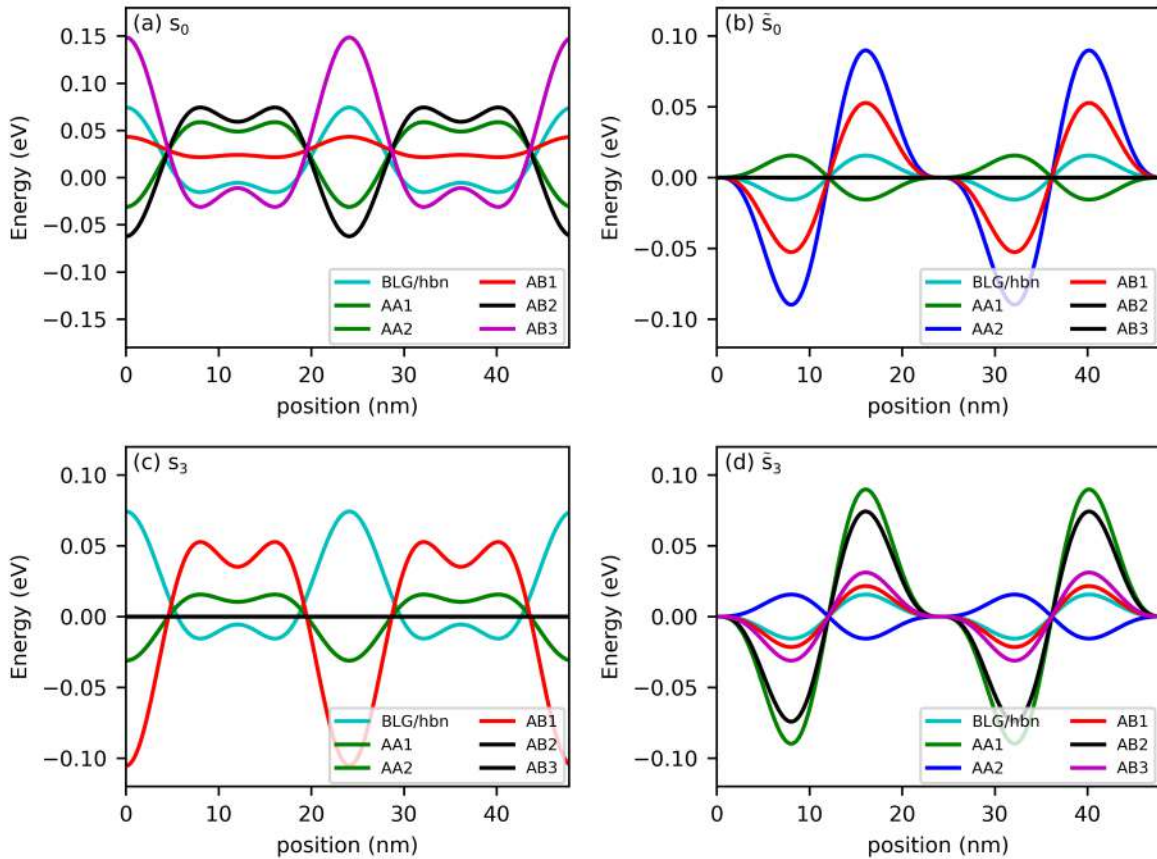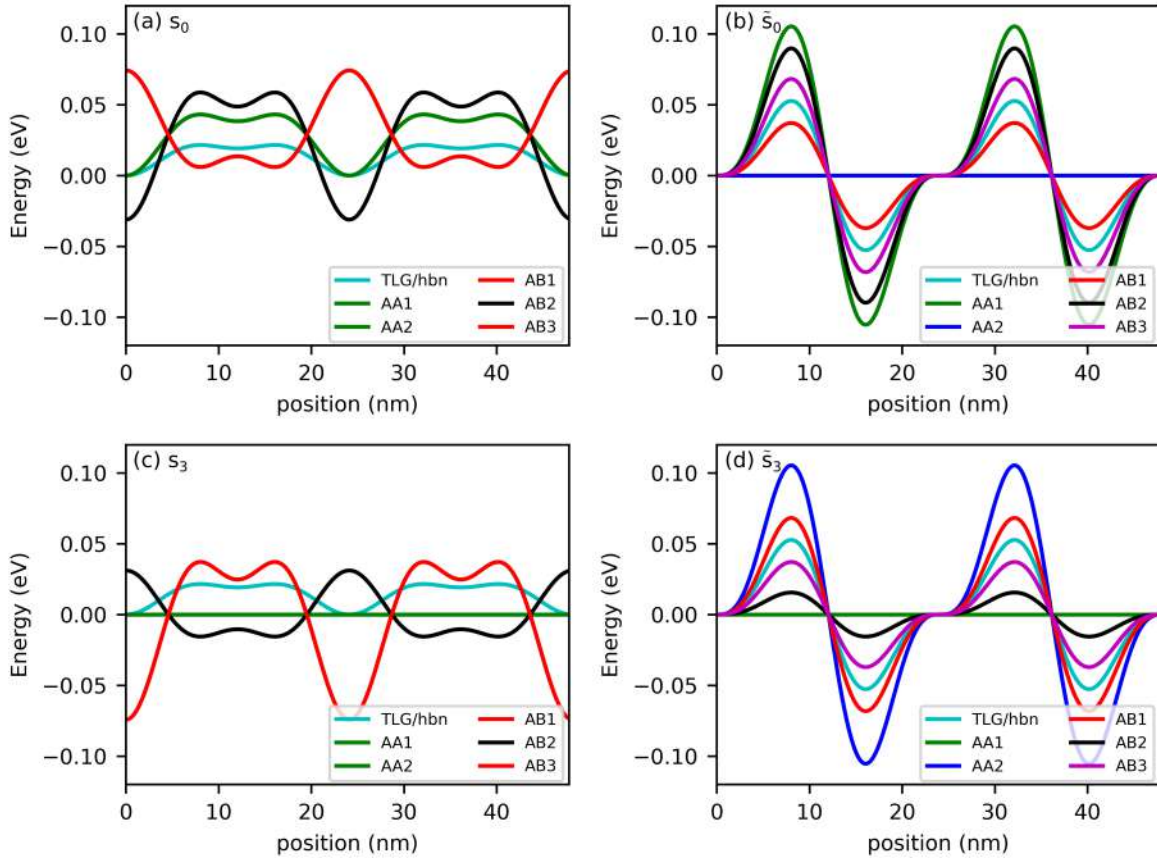

Figure 3. Cut along the y-axis of the different components of the 2D moiré potential of the encapsulated BLG configurations for 2 times the period. The cut goes through the maxima of the potentials. Shown are the (a) s_0 term, (b) $\tilde{s}_0$ term, (c) s_3 term, and (d) $\tilde{s}_3$ term.

Figure 4. Cut along the y-axis of the different components of the 2D moiré potential of the encapsulated TLG configurations for 2 times the period. The cut goes through the maxima of the potentials. Shown are the (a) s_0 term, (b) $\tilde{s}_0$ term, (c) s_3 term, and (d) $\tilde{s}_3$ term.

2. TLG with different coupling to hBN

In this section we perform the same atomistic tight-binding calculations as shown in Figure 2 in the main text for unrelaxed ABC-stacked trilayer graphene on hBN, but with a modified set of parameters describing the graphene/hBN interfaces. We compare graphene/hBN parameter sets as used in the BLG configurations by using the Slater-Koster type functions or the LDA parametrization. For the ABC stacked trilayer we use the LDA parameters shown in the main text. The relevant difference between these two sets is the value of γ_1, 0.48eV for the Slater-Koster set versus 0.348eV for the LDA set.

The resulting electronic band-structures are shown in figure 5 both with and without gating. The bands where the LDA parameters are used (red) show a smaller gap at both the PDP and SDP when no gating is applied and has a larger bandwidth in the plot with gating than the bands where the Slater-Koster parameters are used (blue). From figure 5 it is clear then that the occurrence of isolated flat bands depend on the exact parameters used for the coupling of graphene and hBN, especially when the effective
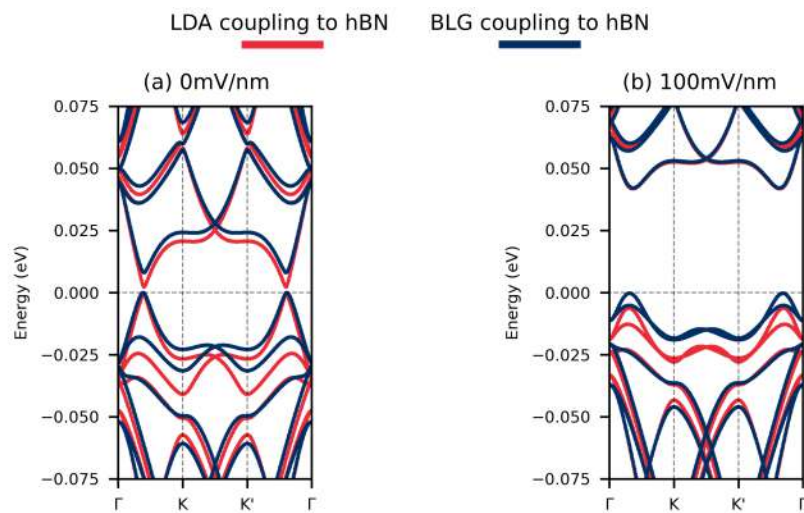
Figure 5. Electronic band-structures for the TLG/hBN system where a different parameter set is used for the hoppings between graphene and hBN and within the hBN layer. In red the LDA set is used, in blue the same parameter set as for the BLG configurations in the main text is used. (a) Has no applied electric field. (b) Has an applied electric field of 100mV/nm.

gaps are small, which is the case here.

3. Density of states as a function of gating

Here we present the density of states along the $\Gamma - K - K' - \Gamma$ path for all the BLG systems in figure 6 and all the ABC TLG systems in figure 7 both for which relaxation effects are present. The gating is implemented as described in the methods section in the main text. From these plots, gaps in the spectrum can be easily identified as well as their behaviour when gating is applied. The plots for graphene on a single hBN layer are skewed upwards due to the applied potential no longer being symmetric around zero when only considering the graphene layers.
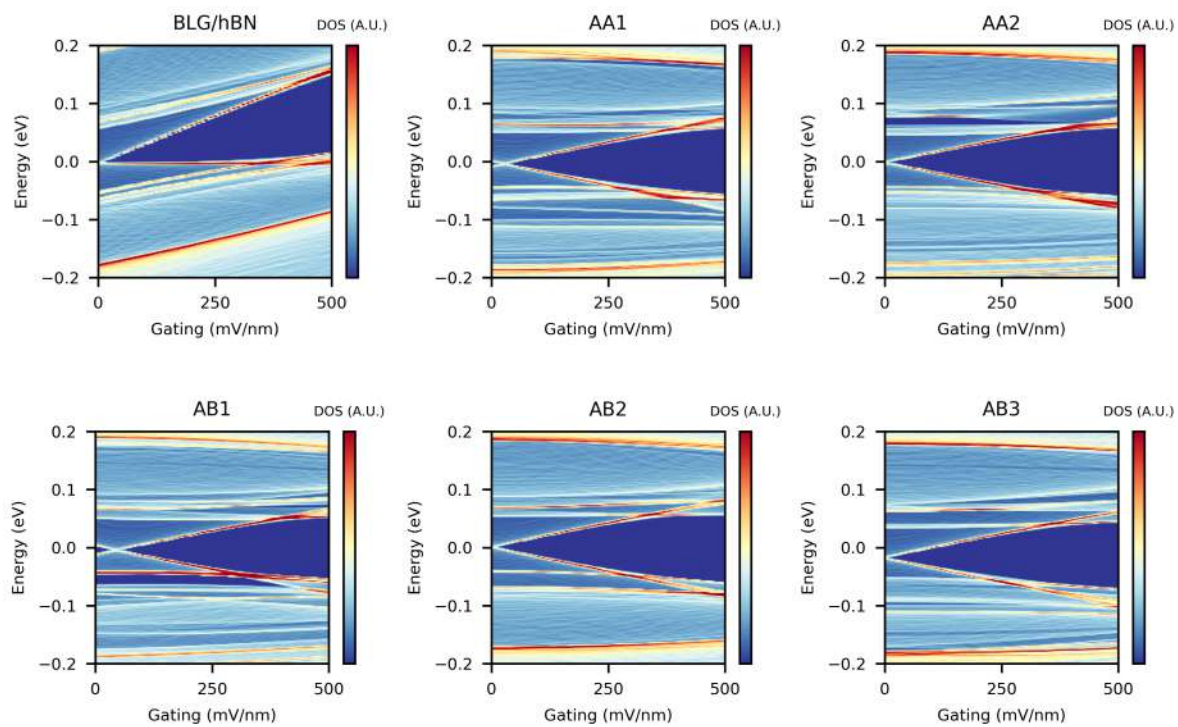

Figure 6. Dos as a function of gating at energies ranging from -0.2eV to 0.2eV for AB bilayer graphene systems. The DOS is taken along $\Gamma - K - K' - \Gamma$ and is given in arbitrary units.
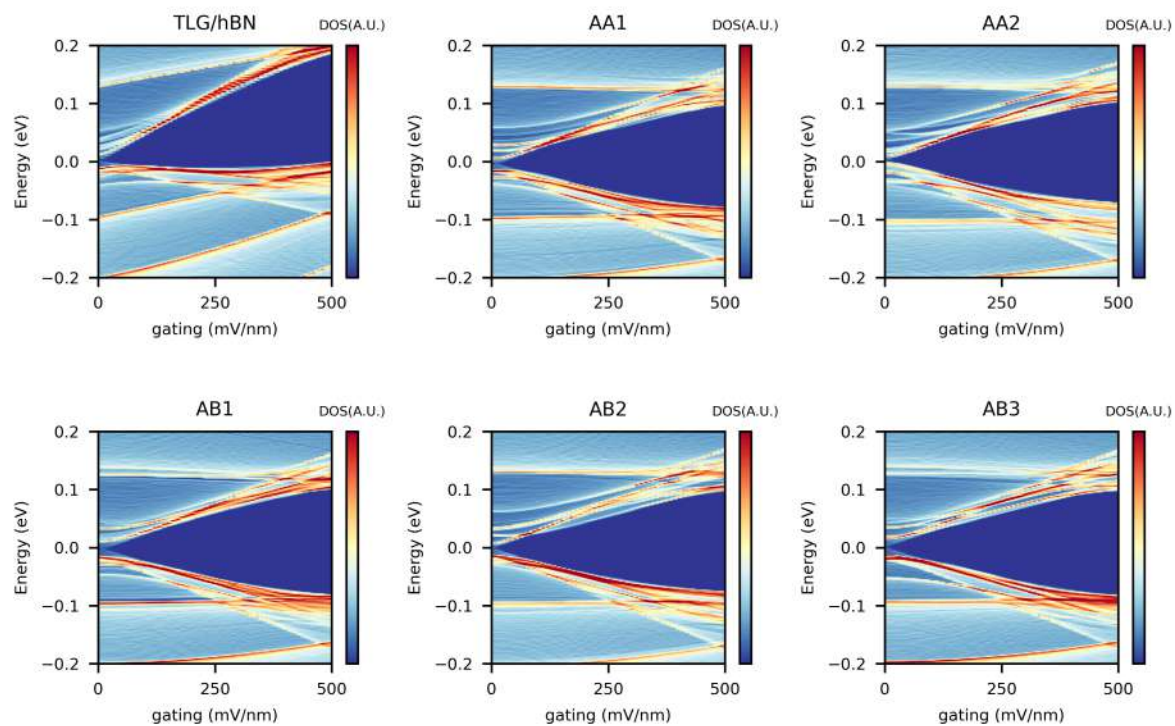
Figure 7. Dos as a function of gating at energies ranging from -0.2eV to 0.2eV for ABC trilayer graphene systems. The DOS is taken along $\Gamma - K - K' - \Gamma$ and is given in arbitrary units.

4. Average DOS per sublattice

In figure 8 the average DOS per sublattice of graphene is shown, where A1 and B2 are the low-energy (non-dimer) sites and B1 and A2 are the high-energy (dimer) sites. The different dips in the DOS correspond with the formation of the SDPs. It is also interesting to note that for systems with broken inversion symmetry, the layer degeneracy is broken as the DOS for the dimer and non-dimer sites are no longer identical.
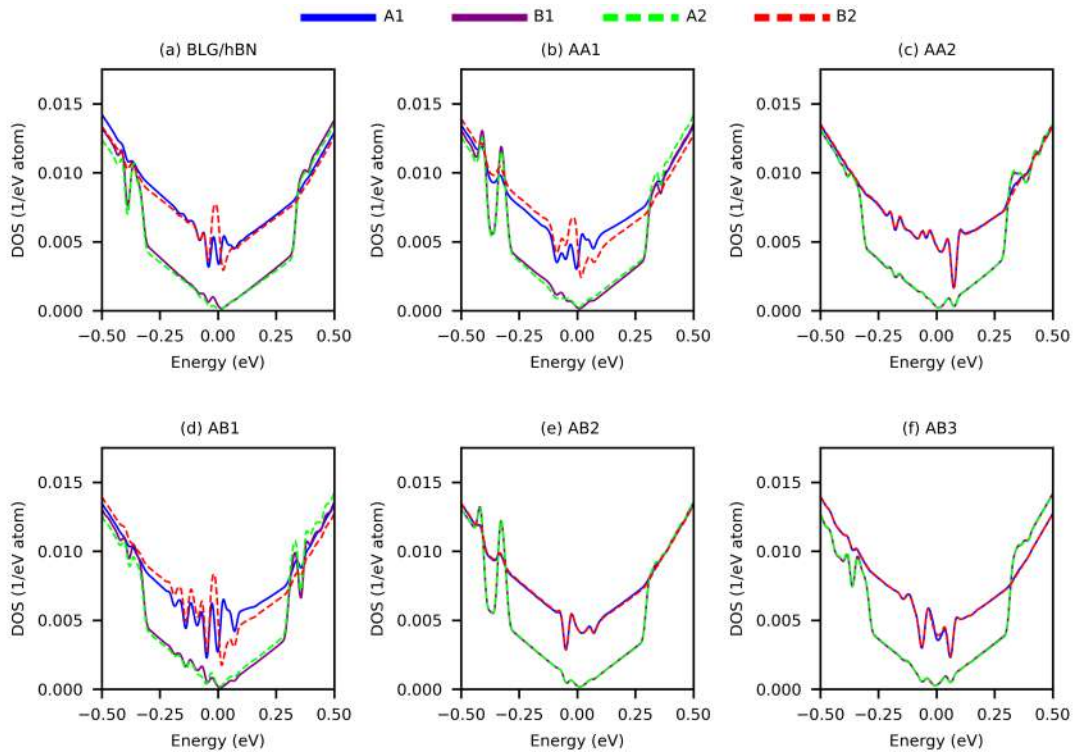

Figure 8. The average DOS per sublattice of bilayer graphene for the whole moiré supercell for the different configurations.

5. In-plane strain

In this section we provide maps of the in-plane strain that is present in the different systems. The local stacking regions are indicated in each map. Three distinct local stacking configurations can be defined, AA which has both boron and nitrogen on top of a carbon atom, AB which has boron on top of carbon and nitrogen in the centre of a carbon ring and AB' which has nitrogen on top of carbon with boron in the centre of a carbon ring. As mentioned in the main text, the AB stacked regions are expanded in the graphene layer and contracted in the hBN layer due to it being the most energetically favourable stacking configuration, this way the area containing this configuration is maximized. The strain is accumulated in surrounding regions in the shape of domain walls with AA and AB' stacked regions [6]. As is clear from figures 9 and 10, the in-plane strain is almost entirely determined by the local stacking between graphene and hBN and the in-plane strain in neighbouring graphene layers do not affect each other. This is also clearly visible since the middle graphene layer in the TLG systems has strongly reduced in-plane strain as it neighbours no hBN layer.
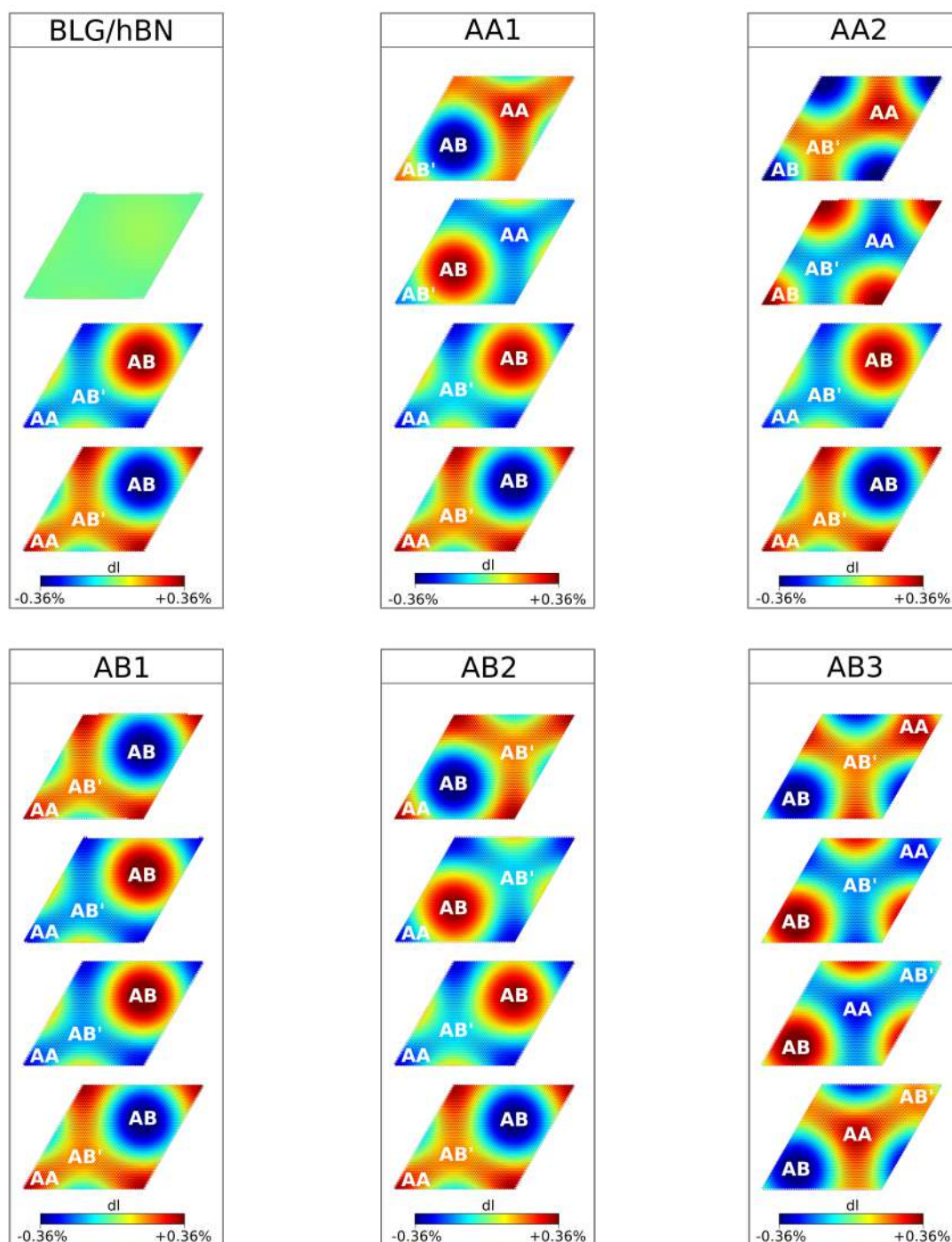
Figure 9. Maps for the BLG systems indicating the in-plane strain due to relaxation effects as a percentage of the original bond length, which are a_{gr} 0.142nm for graphene and $a_{hBN} = 1.018\ a_{gr}$ for hBN.
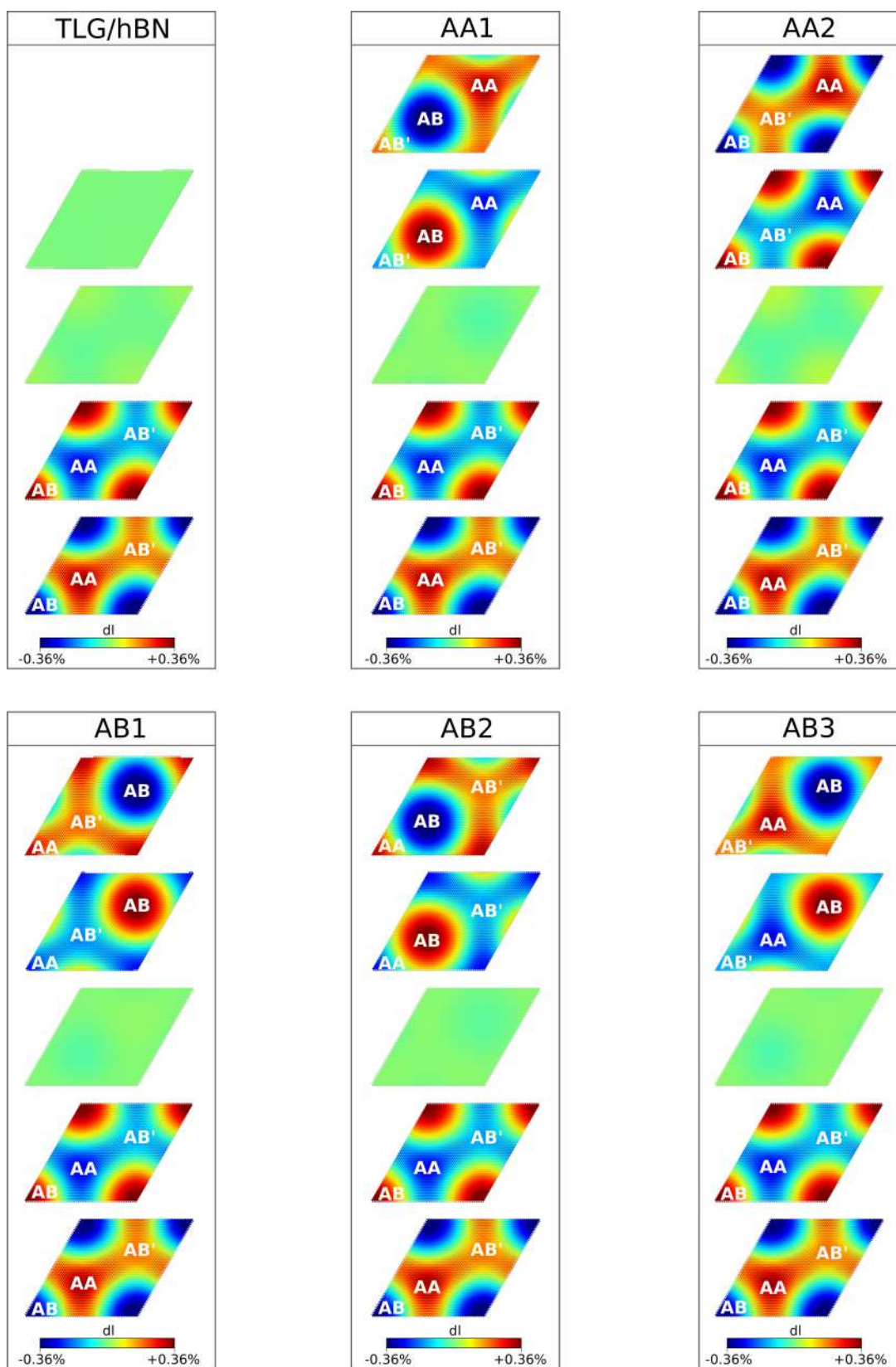
Figure 10. Maps for the TLG systems indicating the in-plane strain due to relaxation effects as a percentage of the original bond length, which are a_{gr} 0.142nm for graphene and $a_{hBN} = 1.018\ a_{gr}$ for hBN.

6. Pseudo-magnetic field due to in-plane strain

Here we show the pseudo-magnetic field (PMF) that emerges due to the in-plane strain caused by relaxation effects. The values of the PMF for all systems are on the order of 9 T, being different than the 40 T which was found in Ref. [7]. Here the PMF is entirely dependent on the local stacking between graphene and hBN so that the PMF for all systems can be further extrapolated from figure 11.
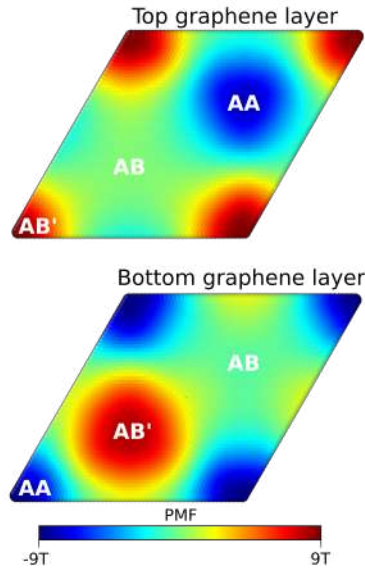

Figure 11. The pseudo-magnetic field on the low-energy sites in the graphene layers for the AA1 BLG system as a result of in-plane strain.

[1] Wallbank J R, Patel A A, Mucha-Kruczynski M, Geim A K and Fal'ko V I 2013 *Phys. Rev. B* **87** 245408 URL https://doi.org/10.1103/PhysRevB.87.245408

[2] McCann E and Koshino M 2013 *Rep. Prog. Phys.* **76** 056503 URL https://iopscience.iop.org/article/10.1088/0034-4885/76/5/056503

[3] Koshino M and McCann E 2009 *Phys. Rev. B* **80** 165409 publisher: American Physical Society URL https://link.aps.org/doi/10.1103/PhysRevB.80.165409

[4] Wallbank J R, Mucha-Kruczyński M, Chen X and Fal'ko V I 2015 *Ann. Phys. (Berlin)* **527** 359–376 URL https://onlinelibrary.wiley.com/doi/10.1002/andp.201400204

[5] Moon P and Koshino M 2014 *Phys. Rev. B* **90** 155406 URL https://doi.org/10.1103/PhysRevB.90.155406

[6] Argentero G, Mittelberger A, Reza Ahmadpour Monazam M, Cao Y, Pennycook T J, Mangler C, Kramberger C, Kotakoski J, Geim A K and Meyer J C 2017 *Nano Lett.* **17** 1409–1416 URL https://doi.org/10.1021/acs.nanolett.6b04360

[7] Jung J, Laksono E, DaSilva A M, MacDonald A H, Mucha-Kruczyński M and Adam S 2017 *Phys. Rev. B* **96** 085442 URL https://link.aps.org/doi/10.1103/PhysRevB.96.085442